An Efficient Transient Temperature Monitoring of Fused Filament Fabrication Process with Physics Based Compressive Sensing

Yanglong Lu and Yan Wang*

Woodruff School of Mechanical Engineering, Georgia Institute of Technology, Atlanta, GA 30332

**Corresponding Author:*

801 Ferst Drive NW, Atlanta, GA 30332-0405, USA

yan.wang@me.gatech.edu (Email) +1-404-894-4714 (Tel.)

An Efficient Transient Temperature Monitoring of Fused Filament Fabrication Process with Physics Based Compressive Sensing

Abstract

Sensors play an important role in manufacturing processes. Different types of sensors have been used in process monitoring to ensure the quality of products. As a result, the cost of quality control is rising. Processing a large amount of sensor data for real-time process monitoring is also challenging. Recently, a physics based compressive sensing (PBCS) approach was proposed to reduce the number of sensors and amount of data collection associated with manufacturing process monitoring. PBCS significantly improves the compression ratio from traditional compressed sensing by incorporating the knowledge of physical phenomena in specific applications. In this paper, the PBCS approach is demonstrated with the dynamic process of fused filament fabrication where the constantly changing temperature field needs to be continuously monitored. A transient thermal model for PBCS is formulated. Based on the model, three-dimensional thermal distributions in manufacturing processes can be efficiently monitored by reconstructing distributions from sparse samplings in both spatial and temporal domains. The systematic error from reconstruction can also be predicted and compensated based on a Gaussian process uncertainty quantification approach.

Keywords: Process monitoring; Compressed sensing; Physics based compressive sensing; Process modeling; PDE constrained optimization; Gaussian process

1 Introduction

Sensors have become one of the most important components in manufacturing processes in order to ensure the high quality of products. As manufacturing processes become more complex, more process parameters and system conditions need to be monitored. Many different kinds of sensors have been employed in modern manufacturing systems. As a result, the portion of sensing system life-cycle cost for installation, operation, and maintenance in the overall cost for a manufacturing system is also rising noticeably. Another challenge is that undetected faulty sensors can impose risks on the reliability of manufacturing systems. Inaccurate system information collected by the faulty sensors could lead to wrong decisions on manufacturing operations in real time. Furthermore, the available bandwidth in communication channels for transmission of large volumes of data collected by advanced sensors is always limited. If the data cannot be shared, processed, and used in real time, their original purpose for process monitoring will not be fulfilled. Therefore, there is a practical need for not solely relying on large numbers of advanced sensors to monitor production-scale manufacturing systems.

In the most recent decade, a new sampling and data collection approach, compressive sampling or compressed sensing (CS), was developed. CS is a new approach to capture and represent sparse signals with a reduction of sampling cost. With a small set of collected data samples, the original signal can be reconstructed by numerically solving an inverse problem. If signals can have a sparse representation in the reciprocal space through transformation, e.g. Fourier and wavelet transforms, the reconstruction can be fairly precise when the number of non-zero coefficients in the reciprocal space is small (i.e. *sparse*) and the transformation and projection operations are not correlated (i.e. *incoherent*). Traditional CS can reduce the cost associated with data collection. However, the compression is achieved purely by exploring correlation within data collected by a sensor. This pure data-driven approach cannot achieve the compression ratio at a high level.

Recently, a physics based compressive sensing (PBCS) (Lu and Wang, 2018) was proposed to improve the compression ratio from traditional CS by incorporating the domain knowledge of physics in applications. As few as four thermal readings are needed to reconstruct the complete three-dimensional (3D) temperature field using the PBCS approach. The compression ratio was increased significantly from traditional CS. In this paper, PBCS is used to monitor the transient temperature field in fused filament fabrication (FFF) process. Based on the formulation of the transient thermal model, 3D thermal distributions in manufacturing processes can be efficiently monitored by reconstructing distributions from sparse sampling in both spatial and temporal domains. Reconstructed temperature distributions are helpful to identify some defects of printed parts. For example, temperature gradients on the top surface can be used to indicate gaps or holes in the top layers if there are some sharp changes of temperature gradients. In the real-time monitoring, the cooling rate can also be estimated, which is used to predict undesired residual stresses and identify shrinkage. Four temperature readings at one time step can be used to reconstruct the temperature field at other time steps. It is also demonstrated that the systematic error from reconstruction can be predicted and compensated with data-driven uncertainty quantification approaches such as Gaussian process regression.

In the remainder of the paper, the background of additive manufacturing process monitoring and classical compressed sensing is introduced in Section 2. The framework of PBCS for measuring and reconstruction of transient temperature distribution is proposed in Section 3. The physical experiments and measurement results are shown in Section 4. Its application to transient temperature monitoring is demonstrated with the FFF or material extrusion process and compared with high-resolution experimental measurements in Section 5. The PBCS method for real-time monitoring is demonstrated in Section 6. A Gaussian process approach to predict and compensate the systematic errors is proposed in Section 7.

2 Background

In this section, the background of additive manufacturing process monitoring is given. Traditional compressed sensing is also introduced.

2.1 Additive manufacturing process monitoring

Process monitoring in additive manufacturing (AM) is important to ensure the quality of products. Various techniques and sensing systems have been applied to monitor AM processes. In selective laser melting (SLM) process, infrared (IR) thermal camera has been used to monitor the surface and the melt material temperatures (Wegner and Witt, 2011; Rodriguez *et al.*, 2015; Lane *et al.*, 2016), the laser powder interaction zone (Bayle and Doubenskaia, 2008), and parameter deviations in the building process (Krauss *et al.* 2012). Temperature files at different locations can be used to analyse the correlations between process parameters and part properties based on temperature gradients and heating or cooling rates. Understanding the effect of process parameters is useful for simulation, monitoring and control. Hu *et al.* (2002 and 2003) set up a thermal imaging system with a high-speed IR camera coaxially to the laser beam to acquire the temperature field of the melt pool. The part quality can be improved by controlling the heat input based on the measured temperature profile. In addition to the IR thermal camera, optical cameras such as charge coupled device (CCD) and complementary metal oxide semiconductor (CMOS) were also integrated into SLM to detect defects in the process. Foster *et al.* (2015) listed three categories of defects such as defects caused by the machine parameters or powder feedstock used in the build, defects resulting from the build plan, and defects due to miscalibration or damage to the equipment. These defects can be monitored by various sensors. Craeghs *et al.* (2011) studied the effect of geometric factors in the SLM process and found that three types of local geometry around the melt pool, including adjacent scan vectors, overhang zones, and acute corners, have significant influence on the processing behaviour. Optical cameras have been used to observe the melt pool and interpret melt pool radiation (Lott *et al.*, 2011; Doubenskaia *et al.*, 2016), errors in the process stability because of insufficient power and poor supports (Kleszczynski *et al.* 2012), surface temperature profile (Chivel and Smurov, 2010; Islam *et al.*, 2013), geometric defect (Grasso *et al.*, 2017), and surface distortion (Land *et al.*, 2015; Zhang *et al.*, 2016). Rombouts *et al.* (2006) employed a coaxial CMOS camera system to monitor the building process of parts with different materials. The effects of elements such as oxygen, carbon, silicon, titanium and copper on the quality of iron-based objects were studied. Other sensors have also been applied to monitor the SLM process. For example, Kanko *et al.* (2016) and Neef *et al.* (2014) used low-coherence interferometry imaging systems to monitor melt pool. Rieder *et al.* (2014) applied ultrasound to detect the residual stress accumulation in SLM process. Wasmer *et al.* (2017) used the acoustic emission sensor to monitor machine states.

In FFF or material extrusion process, thermal IR camera was applied to measure temperature distribution of printed parts and printing environments. Dinwiddie *et al.* (2013) used two approaches to setup cameras to monitor the complete printing environment and heated extrusion head with a close-up view respectively. The temperature gradient of the part and the effect of different designs of extrusion heads are also analysed. The optical camera was used to monitor the FFF process for different purposes. Baumann and Roller (2016) listed five classes of detects such as the detachment, the missing material flow, the deformed object, surface errors and the deviation from the model. They developed an optical system to detect three out of those five defects. Nuchitprasitchai *et al.* (2017) designed single- and two-camera systems to detect a clogged nozzle, loss of filament, and an incomplete project. They also developed the 3D reconstruction algorithm from two images captured by the two-camera system. Instead of monitoring the printed part, Greeff *et al.* (2017) measured the filament slippage, which is the difference between the filament feed gear speed and the filament speed with a low-cost microscope video camera. The part quality can be improved by controlling the flow rate. Rather than cameras, other sensors and techniques have also been used in monitoring the FFF process. Wu *et al.* (2016a, 2016b, 2017) employed the acoustic emission technique to identify normal and abnormal states of machine conditions. Kim *et al.* (2015) detected the deposition status by measuring the current of the filament feed pump. Rao *et al.* (2015) developed a heterogeneous sensor array including thermocouples, accelerometers, an IR camera and a real-time miniature video borescope to monitor the FFF process. Other techniques used in monitoring the FFF process include augmented reality technique (Ceruti *et al.*, 2017), ultrasonic inspection technique (Cummings *et al.*, 2017), fiber Bragg grating sensor (Kousiatza and Karalekas, 2016), and laser triangulation system (Faes *et al.*, 2014).

Sensing systems were also used to ensure the build quality of other AM processes, e.g. the applications of thermal infrared camera for electron beam melting (Price *et al.*, 2012), spectroscopy in direct laser deposition process (Bartkowiak, 2010), a sensor array including a photodiode, a pyrometer and a CCD camera for laser cladding process (Bi *et al.*, 2006; 2007), and an IR thermometer used in monitoring laser engineered net shaping process (Hua *et al.*, 2008; Tan *et al.*, 2010).

2.2 Compressive sampling or compressed sensing

Compressive sampling or compressed sensing (Candes and Tao, 2006; Donoho, 2006) was developed to recover one- or two-dimensional signal with limited collected data if the signal has sparse representation. Suppose that the original signal is represented in a discrete format as vector $\boldsymbol{s}$. It can be represented in the reciprocal space via transformation as $\boldsymbol{s} = \boldsymbol{\Psi\gamma}$ where $\boldsymbol{\Psi}$ is the matrix representation of transformation (or basis matrix) and $\boldsymbol{\gamma}$ is the vector of coefficients. The size of the original signal vector $\boldsymbol{s}$ is *N*. The size of the coefficients $\boldsymbol{\gamma}$ could be similar to *N*, however, only *K* of them are non-zero (*K*<*N*). That is, $\boldsymbol{\gamma}$ is *K*-sparse. When the signal is projected into another space to $\boldsymbol{y} = \boldsymbol{\Phi s}$ with reduced dimension M ($M<N$) via a projection (or measurement) matrix $\mathbf{\Phi}$, the recovery of the original signal from the measured data is to solve the linear equations $\boldsymbol{y} = \mathbf{\Phi}\boldsymbol{s} = \mathbf{\Phi\Psi}\boldsymbol{\gamma} = \mathbf{\Theta}\boldsymbol{\gamma}$. Loosely speaking, because of the K-sparsity, solving $\boldsymbol{y} = \mathbf{\Theta}\boldsymbol{\gamma}$ first then recovering by $\boldsymbol{s} = \mathbf{\Psi}\boldsymbol{\gamma}$ provides more accurate recovery than solving $\boldsymbol{y} = \mathbf{\Phi}\boldsymbol{s}$ directly. The recovery can be precise when the coefficients $\boldsymbol{\gamma}$ is sparse and the transformation and projection operations are incoherent. Compressive sensing has been extensively applied to signal processing (Baraniuk, 2007; Eldar and Kutyniok, 2012), image processing (Gan, 2007; Lustig *et al.*, 2007; Duarte *et al.*, 2008), networked sensing (Haupt *et al.*, 2008), and others.

3 The generic framework of physics based compressive sensing and temperature measurement

The new physics based compressive sensing (PBCS) approach is different from traditional pure data-driven CS developed for generic signals. PBCS can significantly improve the compression ratio with the domain knowledge of physics in applications. The reconstruction process in PBCS is to solve the inverse problem

$$\min \|\boldsymbol{\gamma} - \boldsymbol{\gamma}_0\|_{l_p} \quad (p = 0,1,2) \tag{3.1}$$

$$\text{subject to } \mathbf{u} = \boldsymbol{f}(t, \boldsymbol{\gamma}, \mathbf{u}, \dot{\mathbf{u}}, \ddot{\mathbf{u}}, \nabla\mathbf{u}, \dots) \tag{3.2}$$

where coefficients or parameters $\boldsymbol{\gamma}$ of physical model $\boldsymbol{f}$ need to be recovered, and physical quantities $\mathbf{u}$ as well as their time and spatial derivatives ($\dot{\mathbf{u}}, \ddot{\mathbf{u}}, \nabla\mathbf{u}, \dots$) are described by the model. Different from traditional CS which only relies on linear projection and transformation, here the constraints are physical models. The minimization can be based on the criteria of l_0, l_1, or l_2 norm.

In this work, the PBCS approach is used to monitor the transient temperature distribution. Monitoring the transient temperature distribution is important in AM processes because it affects the residual stresses, microstructure formation, and deformation of produced parts.

3.1 PBCS formulation for transient temperature distribution

The temperature field reconstruction can be formulated as partial differential equation (PDE) constrained optimization problem, which is expressed as

$$\min \quad J(u) := \iiint_{\Omega_0} \frac{1}{2}\left(u(T,x,y,z) - \bar{u}(T,x,y,z)\right)^2 dxdydz \tag{3.3}$$

subject to

$$\frac{c_V}{\kappa} \cdot \frac{\partial u}{\partial t} - \Delta u = 0 \quad \text{in } \Omega \tag{3.4}$$

$$u = p \quad \text{on } \partial\Omega_1 \tag{3.5}$$

$$\frac{\partial u}{\partial n} = g \quad \text{on } \partial\Omega_2 \tag{3.6}$$

$$u(0,x,y,z) = u_0(x,y,z) \quad \text{in } \Omega \tag{3.7}$$

where $\bar{u}(T,x,y,z)$ is the measured temperature at location (x,y,z) at time T and $u(T,x,y,z)$ is the reconstructed temperature. The purpose is to minimize the difference between the measured temperature vector and reconstructed temperature vector at time T in the measurable domain $\Omega_0 \subset \mathrm{R}^3$. The first constraint in Eq.(3.4) is the time-dependent parabolic equation. The second one in Eq.(3.5) is the Dirichlet boundary condition, where p is the specified temperature on the Dirichlet boundary $\partial\Omega_1$. The third one in Eq.(3.6) is the Neumann boundary condition, where Ω_2 is the subdomain of Ω, and n denotes the normal direction to the boundary Ω_2. The fourth one in Eq.(3.7) is the initial condition, which represents the temperature field in the modelling domain Ω when time is zero.

The continuous formulation in Eq.(3.4) is discretized in both spatial and temporal domains. Finite-element discretization in spatial domain and backward Euler discretization in temporal domain are applied, which are described in Sections 3.2 and 3.3 respectively.

3.2 Finite-element discretization in spatial domain

To apply finite-element discretization in spatial domain, the constraint in Eq.(3.4) in steady state becomes

$$\Delta u = 0 \quad \text{in } \Omega \tag{3.8}$$

The weak form for Eqs.(3.5), (3.6) and (3.8) needs to be determined. The boundary condition in this case is a mixture of Dirichlet and Neumann boundary conditions. To approximate u, a finite dimensional space $S^h \subset H^1(\Omega)$ and $V^h \subset V$ are constructed, where $H^1(\Omega)$ is the Sobolev space of functions on Ω, V is the space of test function and the superscript h denotes the discretization parameter chosen as a measure of the mesh size. Let $\{\delta_1, \ldots, \delta_N\}$ be basis functions for the interior of V^h and extend the number of basis functions by ∂N as $\{\delta_{N+1}, \ldots, \delta_{N+\partial\mathrm{N}}\}$ to include the Dirichlet boundary. Then, u needs to be found to satisfy

$$\int_\Omega \nabla u \cdot \nabla v \, d\Omega = \int_{\partial\Omega_2} g \cdot v \, d(\partial\Omega_2) \quad \forall v \in V \tag{3.9}$$

where v's are test functions. Let $u_h \in S^h$, the Dirichlet boundary conditions can be projected into the finite element space S^h so that u in the finite element domain is

$$u_h = \sum_{j=1}^{N} U_j \delta_j + \sum_{j=N+1}^{N+\partial N} U_j \delta_j \tag{3.10}$$

where coefficients U_j's need to be identified to approximate the temperature field. Similarly, $\bar{u}$ in the finite element domain is

$$\bar{u}_h = \sum_{j=1}^{N} \bar{U}_j \delta_j + \sum_{j=N+1}^{N+\partial N} \bar{U}_j \delta_j \tag{3.11}$$

where $\bar{U}_j$ is the measurement at node j. The finite dimensional analogue to Eqs.(3.3), (3.5), (3.6) and (3.8) is to find $u_h \in S^h$, which satisfies

$$\min \quad J(u) \coloneqq \iiint_\Omega \frac{1}{2}\left(u_h(T,x,y,z) - \bar{u}_h(T,x,y,z)\right)^2 dxdydz \tag{3.12}$$

subject to

$$\int_\Omega \nabla u_h \cdot \nabla v_h \, d\Omega = \int_{\partial\Omega_2} g \cdot v_h \, d(\partial\Omega_2) \quad \forall v_h \in V^h \tag{3.13}$$

The discrete cost function can be expressed as

$$\min \quad J(\mathbf{u}) = \frac{1}{2}\mathbf{u}^T\mathbf{M}\mathbf{u} - \mathbf{u}^T\mathbf{b} + \frac{\mathbf{1}}{\mathbf{2}}\bar{u}_h{}^{\mathbf{2}} \tag{3.14}$$

where $\mathbf{M} = \int_\Omega \delta_i \delta_j d\Omega$, $\mathbf{u} = (U_1, \ldots, U_N)^T$, and $\mathbf{b} = \int_\Omega \bar{u}_h \delta_i d\Omega$, where $i, j = 1, \ldots, N$.

The constraint in Eq.(3.13) is equivalent to

$$\int_{\Omega} \nabla\left(\sum_{i=1}^{N} U_i\delta_i\right) \cdot \nabla\delta_j d\Omega + \int_{\Omega} \nabla\left(\sum_{i=N+1}^{N+\partial N} U_i\delta_i\right) \cdot \nabla\delta_j d\Omega = \int_{\partial\Omega_2} g \cdot v_h \, d(\partial\Omega_2) \quad (3.15)$$

which is also

$$\sum_{i=1}^{N} U_i \int_{\Omega} \nabla\delta_i \cdot \nabla\delta_j d\Omega = \int_{\partial\Omega_2} g \cdot v_h \, d(\partial\Omega_2) - \sum_{i=N+1}^{N+\partial N} U_i \int_{\Omega} \nabla\delta_i \cdot \nabla\delta_j d\Omega \quad (3.16)$$

and can be simplified to

$$\mathbf{Ku} = \mathbf{L} \quad (3.17)$$

where $\mathbf{K} = \{\int_{\Omega} \nabla\delta_i \cdot \nabla\delta_j d\Omega\}$ is the conductivity matrix and $\mathbf{L} = \{\int_{\partial\Omega_2} g \cdot v_h \, d(\partial\Omega_2) - \sum_{i=N+1}^{N+\partial N} U_i \int_{\Omega} \nabla\delta_i \cdot \nabla\delta_j d\Omega\}$ is the heat load vector, which combines the Dirichlet boundary values and Neumann boundary values. The necessary condition of optimality is that the first derivative of $J(\mathbf{u})$ in Eq.(3.14) becomes zero, as

$$J'(\mathbf{u}) = (\mathbf{u} - \overline{\mathbf{u}})^T \mathbf{M} = 0 \quad (3.18)$$

where $\overline{\mathbf{u}} = (\overline{U}_1, \dots, \overline{U}_N)^T$, which consists of all measurements. Therefore, the minimization problem in Eq.(3.14) subject to Eq.(3.17) is to find the **L** which minimizes the difference between **u** and $\overline{\mathbf{u}}$.

3.3 Backward Euler discretization in temporal domain

A time discretization of PDE in Eq.(3.4) is based on the backward Euler discretization, as

$$\frac{c_V}{\kappa} \cdot \frac{u_k - u_{k-1}}{\tau} - \Delta u_k = 0 \quad (3.19)$$

where τ is the time step. The finite element discretization of the weak form gives

$$\frac{c_V}{\kappa} \cdot \mathbf{Mu}_k + \tau\mathbf{Ku}_k = \frac{c_V}{\kappa} \cdot \mathbf{Mu}_{k-1} + \tau\mathbf{L} \quad (3.20)$$

Furthermore, Eq.(3.20) can be rearranged to

$$\mathbf{u}_k = \boldsymbol{\alpha}\mathbf{u}_{k-1} + \boldsymbol{\beta}\mathbf{L} \quad (3.21)$$

where $\boldsymbol{\alpha} = ((c_V/\kappa)\cdot\mathbf{M} + \tau\mathbf{K})^{-\mathbf{1}}(c_V/\kappa)\cdot\mathbf{M}$ and $\boldsymbol{\beta} = ((c_V/\kappa)\cdot\mathbf{M} + \tau\mathbf{K})^{-\mathbf{1}}\tau$.

Therefore for *n* time steps, $\mathbf{u}_n$ can be expressed in terms of the initial condition $\mathbf{u}_0$, as

$$\mathbf{u}_n = \boldsymbol{\alpha}^n\mathbf{u}_0 + (\boldsymbol{\alpha}^{n-1}\boldsymbol{\beta} + \boldsymbol{\alpha}^{n-2}\boldsymbol{\beta} + \cdots + \boldsymbol{\alpha}\boldsymbol{\beta} + \boldsymbol{\beta})\mathbf{L} \tag{3.22}$$

Then a first-order system for *n* time steps is obtained as

$$\begin{bmatrix} \mathbf{u}_1 - \boldsymbol{\alpha}\mathbf{u}_0 \\ \mathbf{u}_2 - \boldsymbol{\alpha}^2\mathbf{u}_0 \\ \vdots \\ \mathbf{u}_n - \boldsymbol{\alpha}^n\mathbf{u}_0 \end{bmatrix} = \begin{bmatrix} \boldsymbol{\beta} \\ \boldsymbol{\alpha}\boldsymbol{\beta} + \boldsymbol{\beta} \\ \vdots \\ \boldsymbol{\alpha}^{n-1}\boldsymbol{\beta} + \boldsymbol{\alpha}^{n-2}\boldsymbol{\beta} + \cdots + \boldsymbol{\alpha}\boldsymbol{\beta} + \boldsymbol{\beta} \end{bmatrix}\mathbf{L} \tag{3.23}$$

In addition, the measurement matrix $\boldsymbol{\Phi}$ can be generated as

$$\boldsymbol{\Phi} = \begin{bmatrix} [\boldsymbol{\Phi}_1] & 0 & \cdots & 0 \\ 0 & [\boldsymbol{\Phi}_2] & & 0 \\ \vdots & & \ddots & \vdots \\ 0 & 0 & \cdots & [\boldsymbol{\Phi}_n] \end{bmatrix} \tag{3.24}$$

where $[\boldsymbol{\Phi}_j]$ indicates the locations of measurements at the j^{th} time step. If only the temperature at the final time step is measured and used to reconstruct previous temperature fields, then $\boldsymbol{\Phi}$ can be simplified as $Diag([0 \quad 0 \quad \ldots \quad \boldsymbol{\Phi}_n])$. If only the temperature at the first time step is measured and used to predict future temperature fields, then $\boldsymbol{\Phi}$ will be $Diag([\boldsymbol{\Phi}_1 \quad 0 \quad \ldots \quad 0])$.

The constraints in Eqs.(3.4)-(3.7) after spatial and temporal discretization become

$$\mathbf{u} = \boldsymbol{\Phi}\begin{bmatrix} \boldsymbol{\beta} \\ \boldsymbol{\alpha}\boldsymbol{\beta} + \boldsymbol{\beta} \\ \vdots \\ \boldsymbol{\alpha}^{n-1}\boldsymbol{\beta} + \boldsymbol{\alpha}^{n-2}\boldsymbol{\beta} + \cdots + \boldsymbol{\alpha}\boldsymbol{\beta} + \boldsymbol{\beta} \end{bmatrix}\mathbf{L} + \begin{bmatrix} \boldsymbol{\alpha}\mathbf{u}_0 \\ \boldsymbol{\alpha}^2\mathbf{u}_0 \\ \vdots \\ \boldsymbol{\alpha}^n\mathbf{u}_0 \end{bmatrix} \tag{3.25}$$

The recovery of heat load vector $\mathbf{L}$ from measurement $\bar{\mathbf{u}}$ is based on

$$\bar{\mathbf{u}} = \boldsymbol{\Phi}\begin{bmatrix} \mathbf{u}_1 - \boldsymbol{\alpha}\mathbf{u}_0 \\ \mathbf{u}_2 - \boldsymbol{\alpha}^2\mathbf{u}_0 \\ \vdots \\ \mathbf{u}_n - \boldsymbol{\alpha}^n\mathbf{u}_0 \end{bmatrix} = \boldsymbol{\Phi}\begin{bmatrix} \boldsymbol{\beta} \\ \boldsymbol{\alpha}\boldsymbol{\beta} + \boldsymbol{\beta} \\ \vdots \\ \boldsymbol{\alpha}^{n-1}\boldsymbol{\beta} + \boldsymbol{\alpha}^{n-2}\boldsymbol{\beta} + \cdots + \boldsymbol{\alpha}\boldsymbol{\beta} + \boldsymbol{\beta} \end{bmatrix}\mathbf{L} \tag{3.26}$$

and the reconstruction of the complete temperature fields along time is based on Eq. (3.25) without the measurement matrix $\mathbf{\Phi}$.

In Sections 5 and 6, two scenarios are used to demonstrate PBCS to monitor FFF by applying Eq.(3.26). In the first scenario, the printed part cools down on the printer. It is assumed that the heating environment and geometry of monitored domain remain unchanged. Thus the mass matrix $\mathbf{M}$, the conductivity matrix $\mathbf{K}$, and the heat load vector $\mathbf{L}$ are constant for each time step. In the second scenario, the printing process is monitored in real time. The heating environment is assumed to be constant within two continuous time steps. Since the geometry of the monitored domain is changing, the mass matrix $\mathbf{M}$ and the conductivity matrix $\mathbf{K}$ vary for each time step.

4 Physical Experiments

A Hyrel3D printer is used to print a cube with the size of 45mm×45mm×45mm and a Seek thermal camera is used to measure the temperature field of the part. The material used for printing is Acrylonitrile-Butadiene-Styrene (ABS). The temperature field is measured with PBCS in two scenarios. One is monitoring the cooling process, and the other is real-time monitoring of printing process.

In the first scenario, the printer is paused when the size is 45mm×45mm×5mm, and the part cools down. The thermal camera measures the temperature distribution after the printer is paused. The measured temperature distributions on the top surface at five time steps are shown in Fig. 1. The time interval between two consecutive time steps is 1s.

Image registration is needed to match the measured full images with the reconstructed temperature fields. Affine transformations including scaling, shearing, translation and rotation are performed on the images in Fig. 1, and results are shown in Fig. 2, where the value of each pixel in the grayscale images is linearly mapped to the actual temperature reading. The PBCS to monitor the cooling process is demonstrated in Section 5.

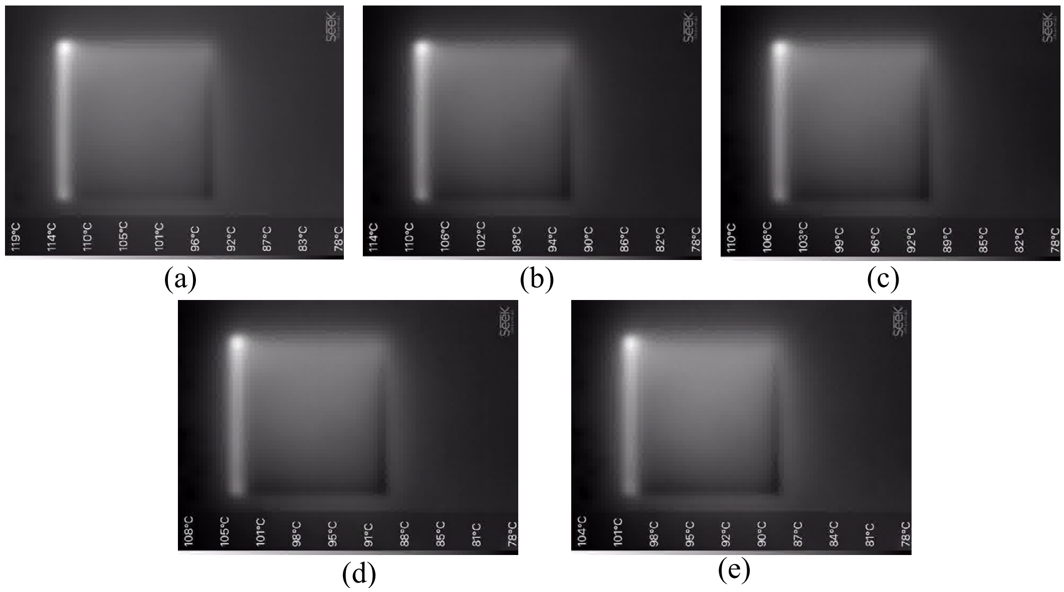

Fig. 1. The full thermal images of the top surfaces at (a) 0s, (b) 1s, (c) 2s, (d) 3s, and (e) 4s.

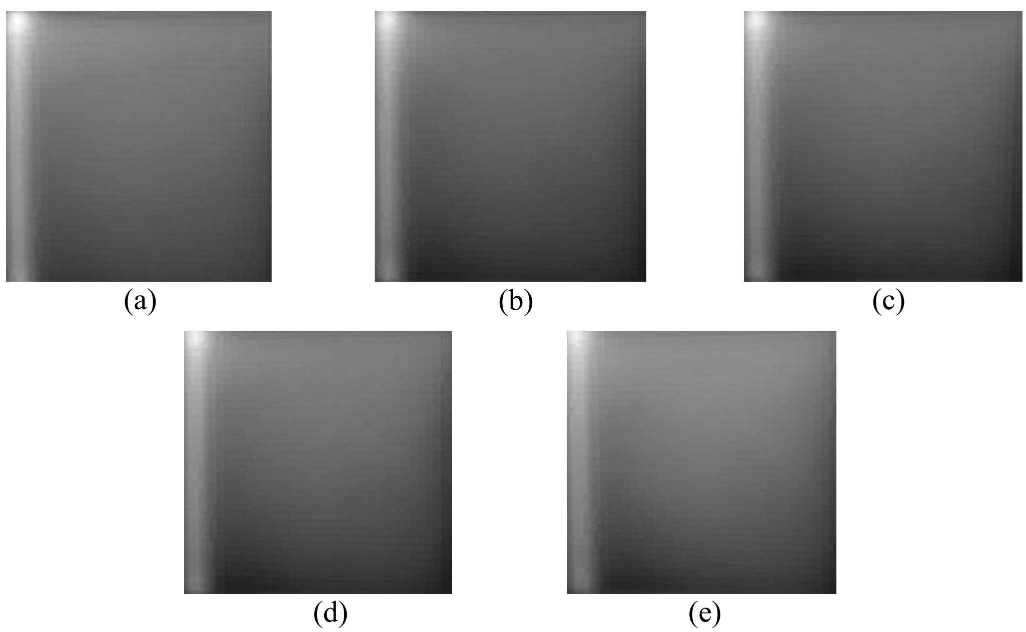

Fig. 2. The measured 2D temperature distributions of top surface after image registration at (a) 0s, (b) 1s, (c) 2s, (d) 3s, and (e) 4s.

In the second scenario, the thermal camera measures the temperature distribution of the part in real time. Measurements at three time steps are selected as shown in Fig. 3(a)-(c). The time interval between two consecutive time steps is 2s. The measured temperature distributions after image registration are shown in Fig. 3(d)-(f). The PBCS for real-time printing process monitoring is demonstrated in Section 6.

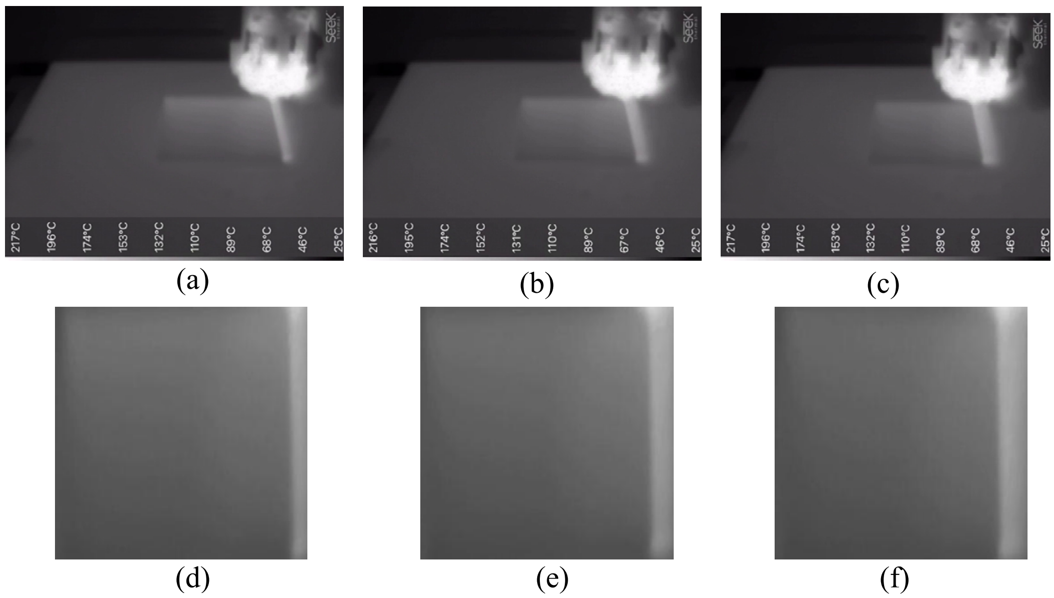

Fig. 3. The full thermal images of the top surfaces at (a) 0s, (b) 2s, and (c) 4s; Meausurements after image registration at (d) 0s, (e) 2s, and (f) 4s.

5 PBCS to Monitor Cooling Process

In the first scenario, the printer is paused and the printed part starts cooling down. The PBCS is used to monitor the change of 3D temperature distribution along time. The model of the printed part is shown in Fig. 4(a), with three newly printed line segments attached on the top left of the part, which matches the case in the experiment. The dimension of each line segment is 0.75mm×45mm×1mm. The extruder pauses at the location of (2.25, 45, 6). Convective boundary conditions are applied to faces F1 to F4 and the heat transfer coefficient is $h_c = 25\ \mathrm{W/m^2 \cdot K}$. Heat flux from the hotbed goes through face F5. The thermal conductivity of ABS is 0.1 W/m·K, the density of 1.04 g/cm^3, and the heat capacity of 1420 J/kg·K.

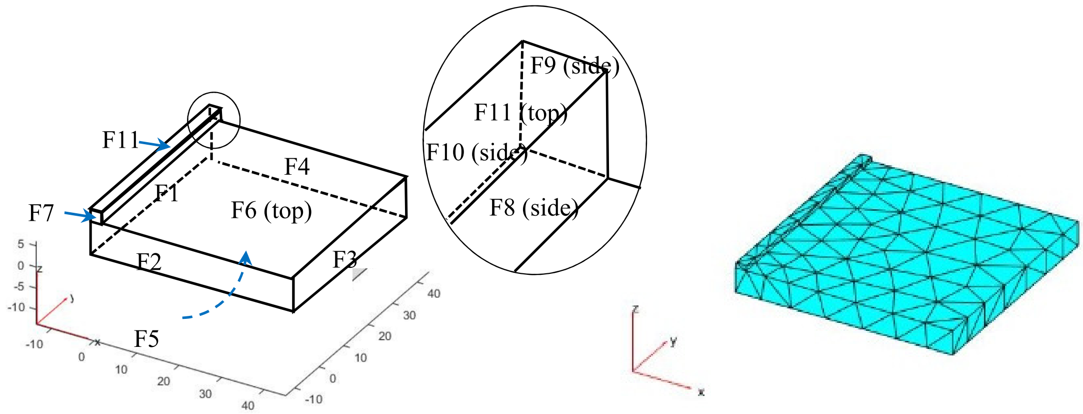

(a) (b)

Fig. 4. (a) The 3D printing domain in material extrusion process, where measurements are mainly taken at side faces F1 to F4; (b) The mesh model

A mesh model is generated as shown in Fig. 4(b). The maximum mesh size is 8 mm, which is the length of the longest edge in the quadratic tetrahedral element. There are a total of 787 nodes in the model. Two cases are tested. The first case is low-fidelity measurement where several temperature readings on each of the four side surfaces are taken, whereas the second one is single-probe measurement where only one reading is taken for each surface. They are described in Sections 5.1 and 5.2 respectively.

The PBCS is performed based on Eq.(3.26), where the initial temperature distribution at time step 0s is needed. The initial temperature distribution is predicted from limited measurements, described as follows. The top surface initial temperature distribution to be measured is shown in Fig. 5(a). The measurement region is divided into two portions. In the subdomain enclosed by the box on the left, the temperature gradient is high in both x and y directions. Eight temperature readings are taken at the top edge (maximum y coordinate value) of the high-gradient left region, with one reading per mm in the x direction. Similarly eight temperatures are taken at the bottom edge (minimum y coordinate value) of the left region. For the purposes of comparison and PBCS error analysis, in this study, all point-wise temperature measurements are taken directly from the IR images shown in Section 4 at the corresponding locations, which is to emulate IR thermometer readings with the consideration of systematic errors between two devices in error analysis. This is to eliminate the effect of systematic error of the IR camera. Other measurement errors are assumed to be smaller than PBCS reconstruction error and not considered here. With the 16 measurements, other temperatures along the y direction in the left region of the top surface then are obtained by linearly interpolating the corresponding top and bottom edge temperatures. For the subdomain on the right of top surface with low gradient, bilinear interpolation is used to predict the 2D temperature distribution from four readings at the respective four corners. After the 2D temperature distribution of the top surface is obtained, the temperatures in the z direction are obtained by linear interpolation between top and bottom surface temperatures, where the bottom surface temperature is assumed to be the same as hotbed temperature 80 °C. As a result, the predicted temperature distribution at time step 0s for the 3D model is shown in Fig. 5(b).

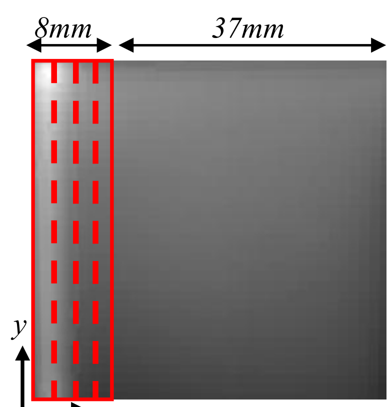

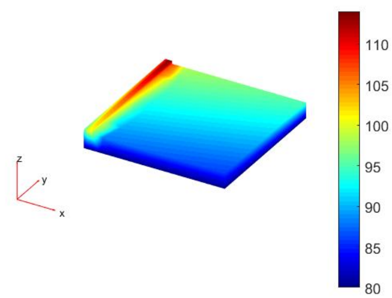

Fig. 5. (a) Temperatures are measured differently in high- and low-gradient regions; (b) Initial temperature distribution at time step 0s after interpolation.

5.1 Low-fidelity measurement

In the first case of the low-fidelity measurement, temperatures on side faces F1 to F4 are measured at time step 4s for reconstruction. At time step 4s, 20 measurements are taken at the similar edge and corner locations in the initial temperature measurements in Fig. 5. Those edge and corner temperatures along with the hotbed temperature are then used to interpolate the 2D distributions on the side faces. Therefore a total of 20 temperature readings are used for the PBCS reconstruction of 787 nodes in the 3D domain. The compression ratio is 787/20=39.35 for one time step reconstruction. The distributions for the previous time steps (steps 1s, 2s, and 3s) are also reconstructed from the reconstructed temperature distribution at time step 4s. Therefore, the compression ratio for all five time steps is (787×5)/(20×2)=98.375. The reconstructed temperature fields at the last four time steps are shown in Fig. 6. The orthogonal matching pursuit algorithm (Tropp and Gilbert, 2007) is used in the heat load recovery.

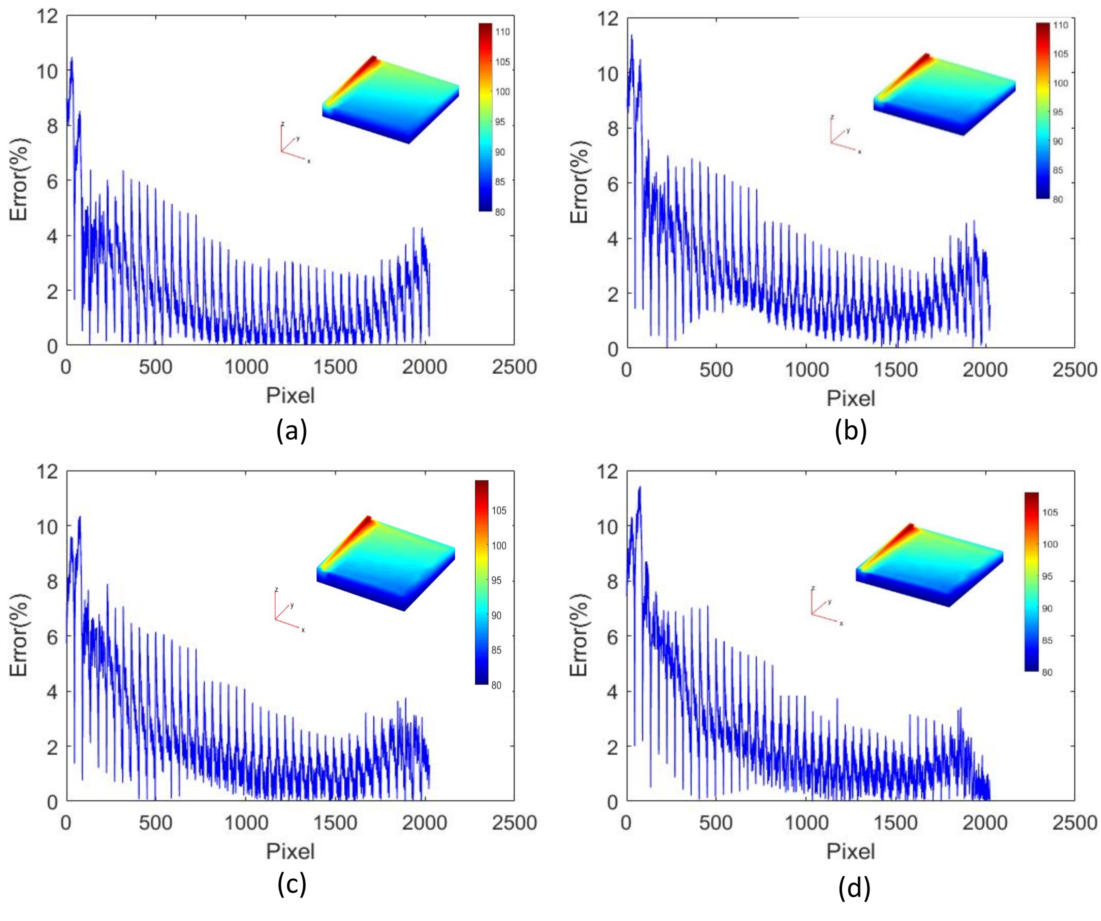

Fig. 6. The measured 3D temperature fields based on the PBCS low-fidelity measurement scheme and PBCS errors at time steps (a) 1s, (b) 2s, (c) 3s, and (d) 4s.

To obtain the reconstruction errors, the reconstructed temperature distributions on the top surface at the four time steps are compared to the experimental measurements in Fig. 2. The 2D temperature distributions on face F6 in Fig. 6 are extracted and interpolated as 2D images with 45 × 45 pixels. The full thermal images after registration are also scaled to 45 × 45 pixels so that they can be compared pixel by pixel. The pixel wise errors from PBCS reconstruction with the low-fidelity measurement are also shown in Fig. 6. The average errors for the four steps are 1.87%, 2.62%, 2.35%, and 2.43% respectively, and the corresponding standard deviations of errors are 1.83%, 1.96%, 2.03%, and 2.27%. Again, the measurement errors associated with the IR camera are assumed to be much smaller than the reconstruction error and not considered in the above comparison. The effect of bias or systematic error of the camera is minimized in the above PBCS error estimation with the readings from the same camera. The PBCS error is mainly contributed by modelling and reconstruction algorithms.

5.2 Single-probe measurement

In the case of single-probe measurement, only one temperature on each face from F1 to F4 is measured. The temperature readings at the centers of four boundary edges at time step 4s are taken as shown in Fig. 7. The temperatures on each face are then assumed to be the same as the measured one. Therefore only four temperature readings are used for the PBCS reconstruction of 3D distributions. The compression ratio for time step 4s is 787/4=196.75. The temperature distribution at the time step 0s is similarly predicted with 20 measurements by the interpolation approach. The temperature distributions at time steps 1s, 2s, and 3s are reconstructed from the reconstruction of time step 4s. Thus the compression ratio for all five steps is (787×5)/(20+4)=163.96. The reconstructed temperature fields at four time steps as well as pixel-by-pixel reconstruction errors are shown in Fig. 8. The average errors for the four steps are 1.87%, 2.63%, 2.42%, and 2.54% respectively, and the corresponding standard deviations are 1.90%, 2.09%, 2.16%, and 2.39%. The reconstruction errors of the single-probe measumrent and the low-fidelity measurement are comparable. This is because the temperature gradients on those side faces are small for this thin part.

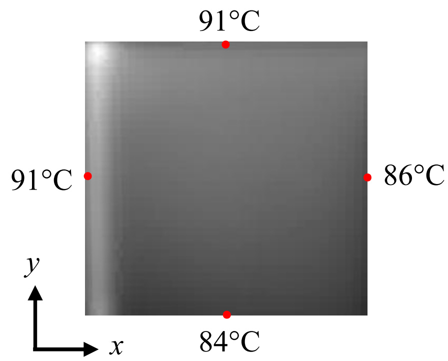

Fig. 7. Single-probe measurements at time step 4s.

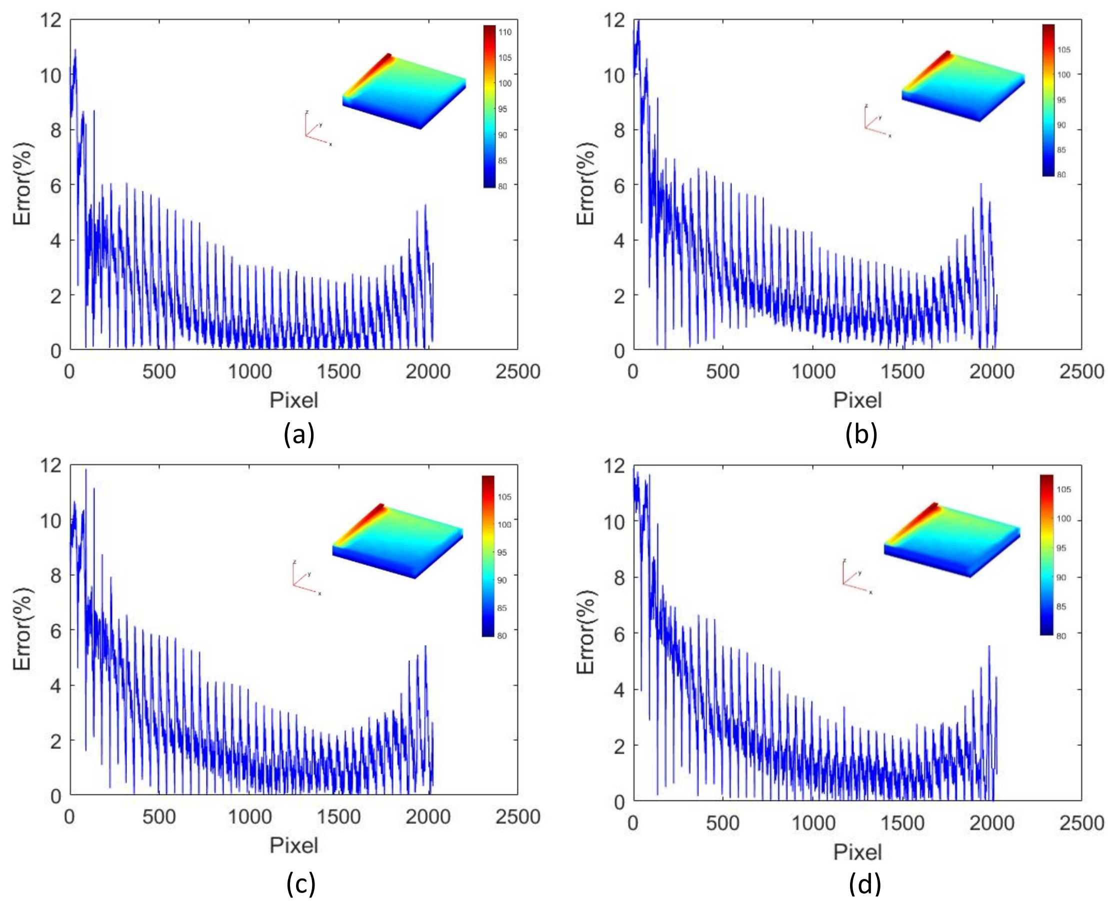

Fig. 8. The measured 3D temperature fields based on PBCS single-probe measurement scheme and PBCS errors at time steps (a) 1s, (b) 2s, (c) 3s, and (d) 4s.

Reconstruction errors in single-probe measurement can come from several sources. First, the physical model of the transient process does not consider the potential variation of geometry, where shrinkage is common and as-fabricated geometry is different from as-designed one. Second, the variation of environmental factors such as heat load during the process affects the temperature field. Third, modelling errors can come from the approximation of surface temperature distribution with only one value. Fourth, the linearization of the original physical model and the numerical treatment during the result interpolation also introduce approximation errors. Additional experimental errors can also be attributed to the image registration process.

6 PBCS for Real-Time Monitoring

In the real-time monitoring of the temperature distribution with PBCS, the geometry of the 3D model in Fig. 4 will change along time. The newly printed segment will be attached on the top surface of the part. In this case, $\boldsymbol{\alpha}$ and $\boldsymbol{\beta}$ in Eq.(3.21) are different for each time step, because the conductivity matrix $\mathbf{K}$ and the mass matrix $\mathbf{M}$ will become larger as time goes by, and more mesh elements are used. Therefore, the birth-and-death element approach is used to generate $\mathbf{K}$ and $\mathbf{M}$ at each time step. At the initial time step, all elements are deactivated by multiplying the conductivity matrix with a factor of 10^{-6} and zero out the load vector and the mass matrix. When a new segment is printed, the corresponding elements will be activated by returning their stiffness, mass, and loads to the original values. In Fig. 3, temperature distributions at three time steps are measured with the time interval 2s. The printing path is shown in Fig. 9, and the temperatures are measured once after one cycle, which consists of two vertical lines. It takes 1s to print a vertical line.

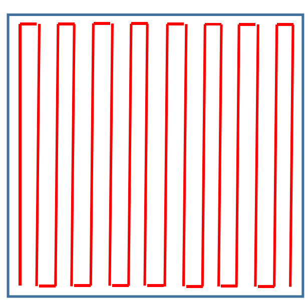

Fig. 9. Visualization of printing path.

Within two continuous time steps, PBCS can be used to recover the heat load vector, and the heat load is assumed to be constant during this time period. The initial temperature shown in Fig. 10(a) is predicted with the same interpolation approach as in Section 5.1 and the low-fidelity measurement from Fig. 3(e) is used to recover the heat load vector. To improve the accuracy of modelling, each vertical line in Fig. 9 is further divided into 9 segments, and each segment has the length of 5 mm and takes 1/9s to print. With the recovered heat load vector, the temperature distribution after each small segment added can be predicted by the birth-and-death element approach. Fig. 10(b)-(i) show some intermediate steps when every two segments are printed for each step, and the time interval is 2/9s. It can be seen that the temperature distribution of the partially printed layer changes as new segments are printed. The temperature distribution of the completed layer does not change much because the time interval is relatively small. Since the heat load vector is recovered with measurements at 0s and 2s, the heat load vector is more accurate to be used to predict temperatures at 2s than the intermediate steps between 0s and 2s. More measurements at the intermediate steps between 0s and 2s can further improve the accuracy.

Fig. 11(a) shows the temperature distribution reconstructed with PBCS at time step 2s. Fig. 11(b) and (c) are PBCS errors by comparing the reconstructed top surface temperature distribution at 2s with direct measurements from the IR camera in Fig. 3(e). It can be found that most errors come from the edge between the newly printed segment and the previously printed layer, which is the intersection between faces F6 and F8 in Fig. 4(a). This is because it is difficult to measure the temperatures at this edge and the size of meshes is not samll enough. The average error excluding the edge is 4.69%, and the corresponding standard deviation of errors is 3.16%.

7 Uncertainty quantification and error compensation

Most errors of PBCS reconstruction are from the physical model, which are due to the applied assumptions and simplifications during the modelling process. These errors can be treated as systematic errors, as differences between the model and physical world. These errors are reducible by introducing more accurate models that incorporate details such as geometry inaccuracy, environmental fluctuation, and multi-physics coupling.

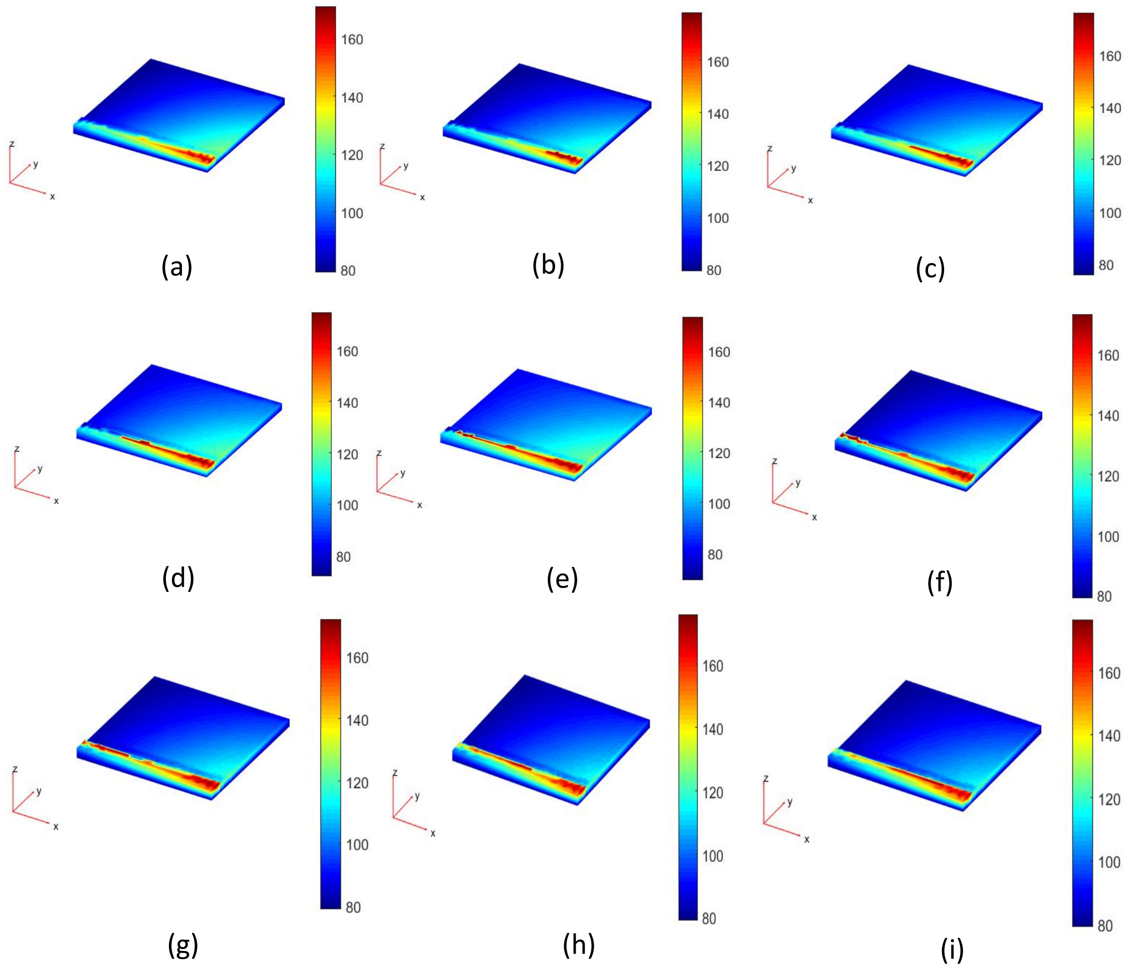

Fig. 10. (a) Initial temperature distribution from interpolation; (b-i) Reconstructed 3D temperature distributions based on the PBCS real-time scheme, with two small segments are printed at each step.

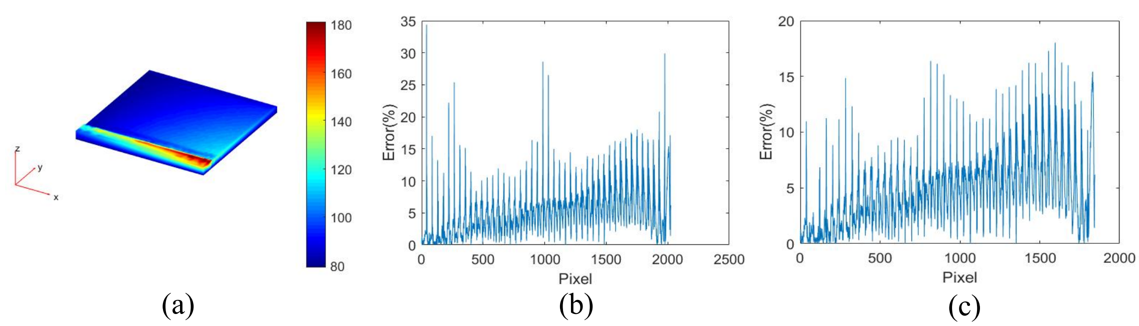

Fig. 11. (a) Measured 3D temperature distribution at 2s based on the PBCS real-time scheme; (b) pixel-by-pixel PBCS errors of the top surface; (c) PBCS errors excluding the F6-F8 edge

The PBCS reconstruction error can be reduced by controlling the systematic error introduced from modeling. Instead of refining the physics-based model, a data-driven approach is taken here to quantify the systematic error. Gaussian process regression (GPR) or kriging is applied. GPR is used to model the difference between the predicted temperature distribution by PBCS and the measured one by full thermal imaging, based on the sampling in both spatial and temporal domains. The GPR model is then used to predict the systematic error for any particular location and time. The predicted error can be applied for the error compensation purpose.

To determine the sample size, the single-probe PBCS reconstruction and full imaging results for the cooling process at time step 4s are first used to construct a two-dimensional GPR model. The second order polynomial basis function and the exponential covariance function are used. The model is constructed by training a set of samples with the least-square error estimation of hyper parameters. To evaluate the GPR model, the coordinates of each pixel in x and y axes are used as the input, and the output is the difference between the single-probe PBCS reconstruction previously extracted from Fig. 8(d) and measurement in Fig. 2(e) at each of the 45×45 pixels. Among a total of 2025 pixels, 200, 500, and 800 sampling points are randomly selected to construct GPR models. As shown in Fig. 12(a)-(c), after error compensation, reconstruction errors can be significantly reduced. More samples can lead to more accurate error prediction, at a cost of longer computational time. When 200, 500, and 800 samples are used, average errors of reconstruction after error compensation are 0.49%, 0.30%, and 0.22% respectively, and the corresponding standard deviations of errors are 0.86%, 0.39%, and 0.33%. Therefore, a sample size of 500 is chosen to construct the complete three-dimensional GPR model with both spatial and temporal dimensions.

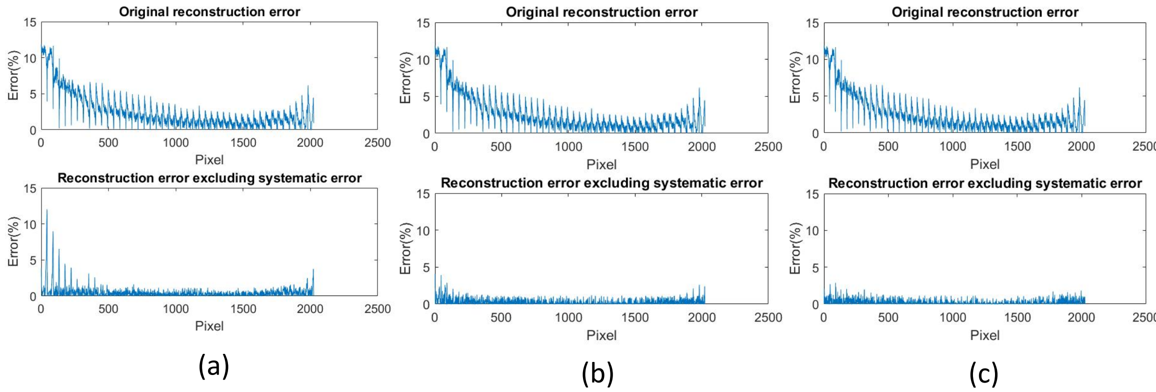

Fig. 12. Comparison of reconstruction errors between before (top row) and after (bottom row) error compensation using GPR models for the time step 4s based on (a) 200 sampling points; (b) 500 sampling points; and (c) 800 sampling points.

A complete three-dimensional GPR model is constructed based on 500 samples in single-probe PBCS reconstruction at each of the time steps except time step 3s, with time as the third dimension of input. The PBCS reconstruction errors before and after error compensation at all pixel positions and all four time steps are shown in Fig. 13. The average errors for the four steps are 0.32%, 0.31%, 0.57 %, and 0.31% respectively, and the corresponding standard deviations of errors are 0.37%, 0.39%, 0.47%, and 0.39%. By comparing average errors and standard deviations of errors in Section 5.2, it is seen that error predictions for all four time steps are significantly reduced. The extent of error reduction at time step 3s is not as much as at other three time steps. This is because error information at time step 3s is not considered in the GPR model construction, and there are not enough samples in the time series. If more time steps are considered and more samples for each time step are taken, the error prediction can be more accurate. In this example, it takes about 2.88 seconds of computational time to build the GPR model and 12.51 seconds to predict errors at all pixels for all four time steps.

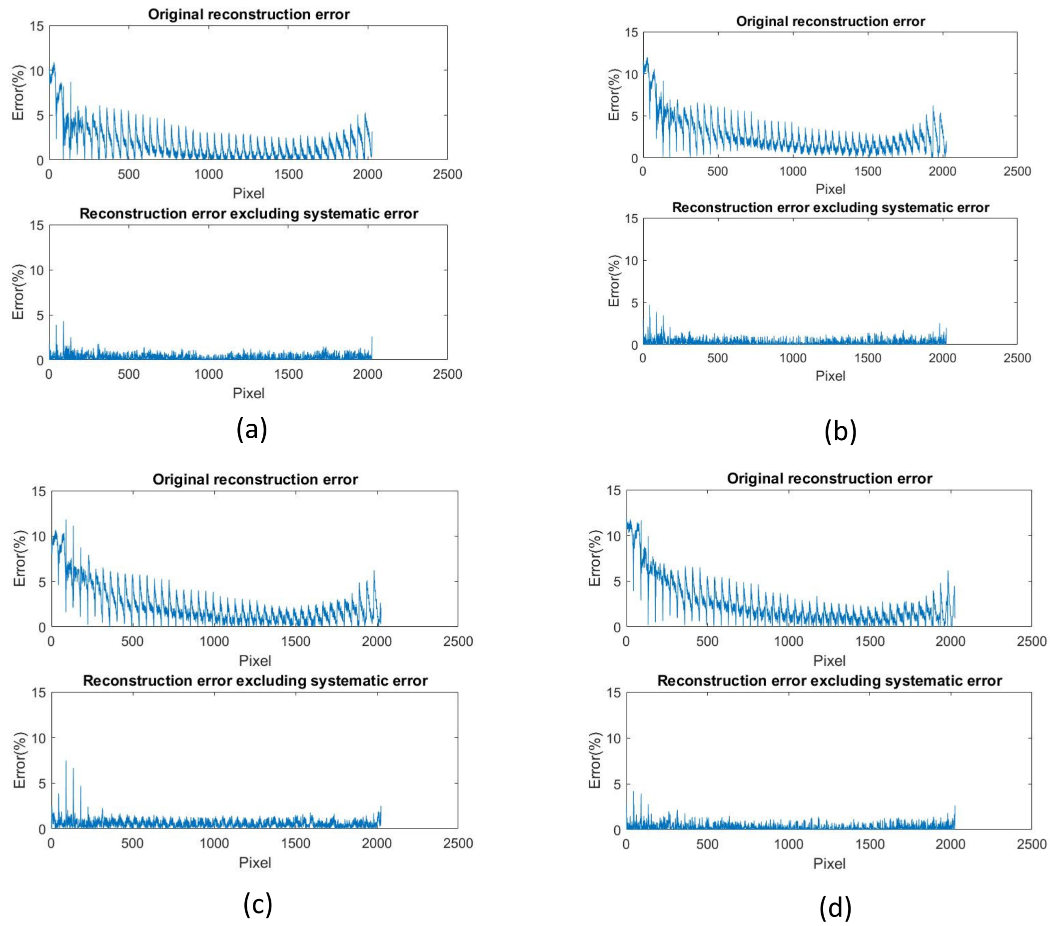

Fig. 13. PBCS reconstruction errors before and after error compensation using Gaussian process regression with time dimension based on 500 samples at four time steps. (a) step 1s: average error reduced from 1.87% to 0.32%; (b) step 2s: average error reduced from 2.63% to 0.31%; (c) step 3s: average error reduced from 2.42% to 0.57 %; and (d) step 4s: average error reduced from 2.54% to 0.31%.

8 Concluding Remarks

A novel process monitoring approach called physics-based compressive sensing has been proposed to efficiently monitor manufacturing processes with low-cost sensors and a limited amount of sensing data. Different from traditional compressed sesning, this method uses the physical knowledge in applications to significantly increase the compression ratio. In this paper, PBCS is used to monitor transient temperature distributions in FFF. It is demonstrated that with the limited measurement of as few as four single-probe temperature readings at one time step, PBCS can be used to recontruct 3D temperature fields at other time steps in the cooling process. In the real-time monitoring process, the PBCS model has different conductivity and mass matrices at each time step. The birth and death element approach can be applied in modeling. The reconstruction errors can be significantly reduced with error predictions from Gaussain process regression. With much less data collection and low-cost sensors deployed, the proposed PBCS shows its distinctive advantages over both traditional imaging based temperature monitoring and traditional compressed sensing in monitoring transient temperature fields.

The accuracy of PBCS largely relies on the accuracy of physical models. To further improve the accuracy, multi-physics models that consider the thermal expansion and shrinkage as well as the imperfect geometry of prints with pores and gaps can be developed. For the error prediction and compensation, the construction of surrogate models can be further studied, such as how to optimize the sampling strategy in both spatial and temporal domains for Gaussian process regression to make the error prediction more efficient, as well as other surrogate modelling methods. In future work, the application of PBCS will be extended to monitor the laser based powder bed fusion, which will be more complex since the laser heat source is involved and the properties of metal powders need to be analysed.

Notes on contributors

Yanglong Lu is a Ph.D. candidate in the George W. Woodruff School of Mechanical Engineering at Georgia Institute of Technology. He received a Bachelor's degree in Mechanical Engineering from Georgia Institute of Technology in 2016. His research focuses on manufacturing process monitoring and process modeling.

Yan Wang is an Associate Professor at the Woodruff School of Mechanical Engineering, Georgia Institute of Technology. He received a Ph.D. degree in industrial engineering from the University of Pittsburgh. He is interested in engineering design, modeling and simulation, and uncertainty quantification. His research work was recognized with multiple conference Best Paper Awards from societies of ASME, IISE, and TMS, as well as a National Science Foundation Early Career Award.

References

Baraniuk, R. G. (2007). Compressive sensing [lecture notes]. *IEEE signal processing magazine*, **24**(4), 118-121.

Bartkowiak, K. (2010). Direct laser deposition process within spectrographic analysis in situ. *Physics Procedia*, **5**, 623-629.

Baumann, F., & Roller, D. (2016). Vision based error detection for 3D printing processes. In *Proc. 2016 International Conference on Frontiers of Sensors Technologies (ICFST 2016)*, **3**, 1–9.

Baumann, F., Schön, M., Eichhoff, J., & Roller, D. (2016). Concept Development of a Sensor Array for 3D Printer. *Procedia CIRP*, **51**, 24-31.

Bayle, F., & Doubenskaia, M. (2008). Selective laser melting process monitoring with high speed infra-red camera and pyrometer. *Fundamentals of Laser Assisted Micro-and Nanotechnologies,* edited by Vadim P. Veiko, Proc. SPIE, **6985***,* 698505.

Bi, G., Gasser, A., Wissenbach, K., Drenker, A., & Poprawe, R. (2006). Identification and qualification of temperature signal for monitoring and control in laser cladding. *Optics and lasers in engineering*, **44**(12), 1348-1359.

Bi, G., Schürmann, B., Gasser, A., Wissenbach, K., & Poprawe, R. (2007). Development and qualification of a novel laser-cladding head with integrated sensors. *International Journal of Machine Tools and Manufacture*, **47**(3), 555-561.

Candes, E. J., & Tao, T. (2006). Near-optimal signal recovery from random projections: Universal encoding strategies? *IEEE transactions on information theory*, **52**(12), 5406-5425.

Ceruti, A., Liverani, A., & Bombardi, T. (2017). Augmented vision and interactive monitoring in 3D printing process. *International Journal on Interactive Design and Manufacturing*, **11**(2), 385-395.

Chivel, Y., & Smurov, I. (2010). On-line temperature monitoring in selective laser sintering/melting. *Physics Procedia*, **5**, 515-521.

Craeghs, T., Clijsters, S., Yasa, E., Bechmann, F., Berumen, S., & Kruth, J. P. (2011). Determination of geometrical factors in Layerwise Laser Melting using optical process monitoring. *Optics and Lasers in Engineering*, **49**(12), 1440-1446.

Cummings, I. T., Bax, M. E., Fuller, I. J., Wachtor, A. J., & Bernardin, J. D. (2017). A Framework for Additive Manufacturing Process Monitoring & Control. In *Topics in Modal Analysis & Testing*, **10**, 137-146. Springer, Cham

Dinwiddie, R. B., Love, L. J., & Rowe, J. C. (2013, May). Real-time process monitoring and temperature mapping of a 3D polymer printing process. *SPIE defense, security, and sensing, International Society for Optics and Photonics*, 87050L.

Donoho, D. L. (2006). Compressed sensing. *IEEE Transactions on information theory*, **52**(4), 1289-1306.

Doubenskaia, M., Grigoriev, S., Zhirnov, I., & Smurov, I. (2016). Parametric analysis of SLM using comprehensive optical monitoring. *Rapid Prototyping Journal*, **22**(1), 40-50.

Duarte, M. F., Davenport, M. A., Takhar, D., Laska, J. N., Sun, T., Kelly, K. E., & Baraniuk, R. G. (2008). Single-pixel imaging via compressive sampling. *IEEE Signal Processing Magazine*, **25**(2), 83.

Eldar, Y. C., & Kutyniok, G. (Eds.). (2012). *Compressed sensing: theory and applications*. Cambridge University Press.

Faes, M., Abbeloos, W., Vogeler, F., Valkenaers, H., Coppens, K., Goedemé, T., & Ferraris, E. (2014). Process monitoring of extrusion based 3D printing via laser scanning. In *Proc. 2014 PMI Conference*, **6**, 363 – 367.

Foster, B. K., Reutzel, E. W., Nassar, A. R., Hall, B. T., Brown, S. W., & Dickman, C. J. (2015). Optical, layerwise monitoring of powder bed fusion. In *Proc. 2015 Solid Freeform Fabrication Symposium, Austin, TX, Aug*, pp. 10-12.

Gan, L. (2007). Block compressed sensing of natural images. In *Proc. 2007 IEEE 15th International conference on digital signal processing*, pp. 403-406.

Grasso, M., Laguzza, V., Semeraro, Q., & Colosimo, B. M. (2017). In-process monitoring of selective laser melting: spatial detection of defects via image data analysis. *Journal of Manufacturing Science and Engineering*, **139**(5), 051001.

Greeff, G. P., & Schilling, M. (2017). Closed loop control of slippage during filament transport in molten material extrusion. *Additive Manufacturing*, **14**, 31-38.

Haupt, J., Bajwa, W. U., Rabbat, M., & Nowak, R. (2008). Compressed sensing for networked data. *IEEE Signal Processing Magazine*, **25**(2), 92-101

Hu, D., Mei, H., & Kovacevic, R. (2002). Improving solid freeform fabrication by laser-based additive manufacturing. *Proceedings of the Institution of Mechanical Engineers, Part B: Journal of Engineering Manufacture*, **216**(9), 1253-1264.

Hu, D., & Kovacevic, R. (2003). Modelling and measuring the thermal behaviour of the molten pool in closed-loop controlled laser-based additive manufacturing. *Proceedings of the Institution of Mechanical Engineers, Part B: Journal of Engineering Manufacture*, **217**(4), 441-452.

Hua, T., Jing, C., Xin, L., Fengying, Z., & Weidong, H. (2008). Research on molten pool temperature in the process of laser rapid forming. *Journal of materials processing technology*, **198**(1), 454-462.

Islam, M., Purtonen, T., Piili, H., Salminen, A., & Nyrhilä, O. (2013). Temperature profile and imaging analysis of laser additive manufacturing of stainless steel. *Physics Procedia*, **41**, 835-842.

Kanko, J. A., Sibley, A. P., & Fraser, J. M. (2016). In situ morphology-based defect detection of selective laser melting through inline coherent imaging. *Journal of Materials Processing Technology*, **231**, 488-500.

Kim, C., Espalin, D., Cuaron, A., Perez, M. A., MacDonald, E., & Wicker, R. B. (2015). A study to detect a material deposition status in fused deposition modeling technology. In *Proc. 2015 IEEE International Conference on Advanced Intelligent Mechatronics (AIM)*, pp. 779-783.

Kleszczynski, S., Zur Jacobsmühlen, J., Sehrt, J. T., & Witt, G. (2012). Error detection in laser beam melting systems by high resolution imaging. In *Proc. 23rd Annual International Solid Freeform Fabrication Symposium*, 975–987.

Kousiatza, C., & Karalekas, D. (2016). In-situ monitoring of strain and temperature distributions during fused deposition modeling process. *Materials & Design*, **97**, 400-406.

Krauss, H., Eschey, C., & Zaeh, M. (2012). Thermography for monitoring the selective laser melting process. In *Proceedings of the Solid Freeform Fabrication Symposium*, pp. 999-1014.

Land, W. S., Zhang, B., Ziegert, J., & Davies, A. (2015). In-situ metrology system for laser powder bed fusion additive process. *Procedia Manufacturing*, **1**, 393-403.

Lane, B., Moylan, S., Whitenton, E. P., & Ma, L. (2016). Thermographic measurements of the commercial laser powder bed fusion process at NIST. *Rapid prototyping journal*, **22**(5), 778-787.

Lott, P., Schleifenbaum, H., Meiners, W., Wissenbach, K., Hinke, C., & Bültmann, J. (2011). Design of an optical system for the in situ process monitoring of selective laser melting (SLM). *Physics Procedia*, **12**, 683-690.

Lu, Y., & Wang, Y. (2018) Monitoring temperature in additive manufacturing with physics-based compressive sensing. *Journal of Manufacturing Systems*, (in press)

Lustig, M., Donoho, D., & Pauly, J. M. (2007). Sparse MRI: The application of compressed sensing for rapid MR imaging. *Magnetic resonance in medicine*, **58**(6), 1182-1195

Neef, A., Seyda, V., Herzog, D., Emmelmann, C., Schönleber, M., & Kogel-Hollacher, M. (2014). Low coherence interferometry in selective laser melting. *Physics Procedia*, **56**, 82-89.

Nuchitprasitchai, S., Roggemann, M., & Pearce, J. M. (2017). Factors effecting real-time optical monitoring of fused filament 3D printing. *Progress in Additive Manufacturing*, 1-17.

Price, S., Cooper, K., & Chou, K. (2012, August). Evaluations of temperature measurements by near-infrared thermography in powder-based electron-beam additive manufacturing. In *Proceedings of the Solid Freeform Fabrication Symposium*, pp. 761-773.

Rao, P. K., Liu, J. P., Roberson, D., Kong, Z. J., & Williams, C. (2015). Online real-time quality monitoring in additive manufacturing processes using heterogeneous sensors. *Journal of Manufacturing Science and Engineering*, **137**(6), 061007.

Rieder, H., Dillhöfer, A., Spies, M., Bamberg, J., & Hess, T. (2014). Online monitoring of additive manufacturing processes using ultrasound. In *Proceedings of the 11th European Conference on Non-Destructive Testing, October*, pp. 6-10.

Rodriguez, E., Mireles, J., Terrazas, C. A., Espalin, D., Perez, M. A., & Wicker, R. B. (2015). Approximation of absolute surface temperature measurements of powder bed fusion additive manufacturing technology using in situ infrared thermography. *Additive Manufacturing*, **5**, 31-39

Rombouts, M., Kruth, J. P., Froyen, L., & Mercelis, P. (2006). Fundamentals of selective laser melting of alloyed steel powders. *CIRP Annals-Manufacturing Technology*, **55**(1), 187-192.

Tan, H., Chen, J., Zhang, F., Lin, X., & Huang, W. (2010). Estimation of laser solid forming process based on temperature measurement. *Optics & Laser Technology*, **42**(1), 47-54.

Tropp, J. A., & Gilbert, A. C. (2007). Signal recovery from random measurements via orthogonal matching pursuit. *IEEE Transactions on information theory*, **53**(12), 4655-4666.

Wasmer, K., Kenel, C., Leinenbach, C., & Shevchik, S. A. (2017). In Situ and Real-Time Monitoring of Powder-Bed AM by Combining Acoustic Emission and Artificial Intelligence. In *International Conference on Additive Manufacturing in Products and Applications*, pp. 200-209. Springer, Cham

Wegner, A., & Witt, G. (2011). Process monitoring in laser sintering using thermal imaging. In *SFF Symposium, Austin, Texas, USA*, pp. 8-10.

Wu, H., Yu, Z., & Wang, Y. (2016a). A new approach for online monitoring of additive manufacturing based on acoustic emission. In *ASME 2016 11th International Manufacturing Science and Engineering Conference*, pp. V003T08A013-V003T08A013.

Wu, H., Wang, Y., & Yu, Z. (2016b). In situ monitoring of FDM machine condition via acoustic emission. *The International Journal of Advanced Manufacturing Technology*, **84**(5-8), 1483-1495.

Wu, H., Yu, Z., & Wang, Y. (2017). Real-time FDM machine condition monitoring and diagnosis based on acoustic emission and hidden semi-Markov model. *The International Journal of Advanced Manufacturing Technology*, **90**(5-8), 2027-2036.

Zhang, B., Ziegert, J., Farahi, F., & Davies, A. (2016). In situ surface topography of laser powder bed fusion using fringe projection. *Additive Manufacturing*, **12**, 100-107.